

Quantification of seismic and acoustic waves to characterize the 2014 and 2015 eruptions of Kuchinoerabujima Volcano, Japan

Haruhisa Nakamichi, Masato Iguchi, Takeshi Tameguri, and Tadaomi Sonoda

Sakurajima Volcano Research Center, Disaster Prevention Research Institute, Kyoto University,

(Received : Oct. 14, 2016 Accepted : May 29, 2017)

Abstract

At Kuchinoerabujima Volcano located in southwest Japan, eruptions occurred on August 3, 2014, and May 29 and June 18, 2015. We evaluated the seismic and acoustic waves excited by these eruptions to characterize the eruptions. First, we estimated the eruption durations at a single station. The durations were 50 s, 6 min, and 6 min for the eruptions on August 3, 2014, and May 29 and June 18, 2015, respectively. The seismic and acoustic waveforms of the 2014 eruption have spindle shapes, while the waveforms of the 2015 eruptions have initial impulsive phases followed by weak arrivals. These three eruptions were phreatomagmatic in nature, as suggested by geological surveys. Second, we estimated the seismic and acoustic energies of the eruptions. The seismic and acoustic energies of the 2014 eruption were 1.88 GJ and 0.21 GJ, respectively. The seismic and acoustic energies of the eruption on May 29, 2015 were 0.36 GJ and 2.2 GJ, respectively; and the seismic and acoustic energies of the eruption on June 18, 2015 were 0.3 GJ and 0.06 GJ, respectively. Third, we estimated the counter single force excited by the eruptions on May 29 and June 18 by using seismic waveform matching at a broadband station. The pulse width and amount of the counter force were lined on the scaling line for a conduit pressure of 6 MPa. For the 2014 eruption, the short duration and spindle-like waveforms may reflect that the eruption was short lived and initially weak, gradually becoming violent and forming fissures, while the 2015 eruptions did not form new fissures.

Keywords : Kuchinoerabujima Volcano, seismic wave, infrasound, energy, single force

1. Introduction

To understand the eruption process and evaluate volcano hazards, it is important to quantify the amount of materials ejected by an eruption. The eruption column height is commonly used as an indicator of the size of an eruption, because the discharge rate of ejected materials is approximately and empirically proportional to the fourth power of the maximum column height (e.g., Sparks et al., 1997; Mastin et al., 2009), and the measurement is timely. However, the column height is strongly influenced by weather conditions, especially the temperature gradient and wind speed (Wilson and Walker, 1987; Glaze and Baloga, 1996; Graf et al., 1999). The maximum column height is usually measured by visual inspections with direct observations or remote cameras and is sometimes verified by radar and satellite measurements. However, it is sometimes difficult to measure the maximum column due to bad weather. A much better estimation of the amount of ejected materials is generally obtained by conducting a geological field survey. Ash-fall deposit measurements are conducted at several points at different distances and azimuths from an eruption source. The volume of the fallout deposit is estimated by using the relationship between the area covered by ash and the thickness of the fall deposit (e.g., Pyle, 1989). However, deposit measurement is labor-intensive and time consuming.

Eruptions generally generate seismic and acoustic waves, the magnitudes and durations of which may reflect not only the total mass and volume of erupted materials but also the explosivity of the eruptions. The amplitude of a volcanic tremor is empirically related to the volume of the ejected materials (McNutt, 1994). McNutt and Nishimura (2008) proposed that the average discharge rate is the value of the total volume of ejected ash from an eruption divided by the duration of an eruption estimated by the eruption tremor. Iguchi (2016) found that the monthly sum of ash weights correlates well with

the monthly sum of the seismic spectral amplitudes for the eruptions of Sakurajima Volcano and constructed an empirical relationship between seismic amplitudes and ejected ash. Prejean and Brodsky (2011) applied the method for estimating the discharge rate using a single force obtained by a seismic waveform analysis (Brodsky et al., 1999) to estimate the column heights of Plinian and Vulcanian eruptions. The discharge rate has been estimated based on infrasound data for explosive eruptions using the relationship between pressure disturbances and density multiplied by the volumetric acceleration from monopole sources (e.g., Johnson et al., 2004). Seismic and acoustic observations can capture signals from eruptions in a timely manner and are, therefore, important in the evaluation of seismic and acoustic waves for obtaining the size of an eruption, its explosivity, and its eruption process.

Kuchinoerabujima Volcano, southwest Japan (Fig. 1), has repeated phreatic and phreatomagmatic eruptions within the past 100 years following the oldest documented eruption in 1841 (Geshi and Kobayashi, 2007). Recently, the volcano erupted once in 2014 and twice in 2015. Since two of the three eruptions occurred during bad weather, it was difficult to evaluate the size and explosivity of the eruptions. It is important to determine the size and explosivity of an eruption as soon as possible even if weather conditions are poor and visual information of the eruption is not available. An observation system near an active volcano generally has a few seismometers and infrasound microphones. In this study, we evaluate the durations of the eruption and released energy based on seismic and infrasound records and the counter single forces for each eruption, which can be related to eruption size, strength, and process, by a single station.

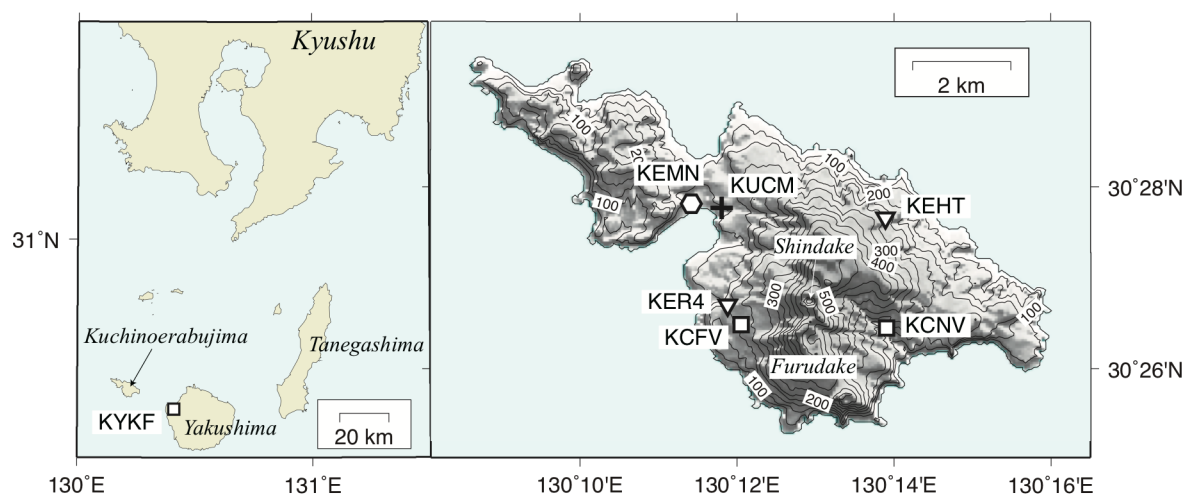


Fig.1. Location of Kuchinoerabujima (Left) and station distribution at Kuchinoerabujima (Right). Web camera located at KEMN, with the lens pointed to Shindake crater. The infrasound sensor (microphone) is located at KUCM (plus mark). Open inverted triangles and open squares indicate seismic stations that belong to the Japan Meteorological Agency and National Research Institute for Earth Science and Disaster Resilience, respectively.

2. The 2014 and 2015 eruptions of Kuchinoerabujima Volcano

Kuchinoerabujima is an andesitic volcanic island located to the south off Kyushu Island, Japan (Fig. 1). Several magmatic eruptions occurred during 1931–34 and 1966–76 at Shindake crater, one of the central cones (Geshi and Kobayashi, 2007). Although no eruption occurred during the 34 years since the fissure eruption east of Shindake crater on September 28, 1980, an explosive eruption occurred at Shindake crater on August 3, 2014 (hereinafter termed the 2014 eruption). Additional explosive eruptions occurred at the crater on May 29 and June 18, 2015, and we refer to them as the 2015A and 2015B eruptions, respectively. The explosive eruptions blew up the hydrothermally-altered materials and also a part of the intruded magma (Geshi et al., 2016). When the 2014 eruption occurred, Typhoon No. 12 was approaching the Ryukyu Islands, including Kuchinoerabujima, and it was windy around the island

with the summit covered with clouds. Fortunately, no one was climbing the summit because of the bad weather (One student party had cancelled their plan to climb). Under the prevailing windy weather conditions, the ash column of the 2014 eruption rose to a height of 0.8 km from the rim of the crater and drifted in the NNE direction, which was witnessed by the distant view camera at station KEMN (Fig. 1) (Japan Meteorological Agency, 2014). The pyroclastic density current (PDC) of the 2014 eruption flowed down to ~2 km from the crater (Geshi et al., 2016). The 2015A eruption occurred during fine weather, and its ash column reached at least 9 km above the crater rim, which was witnessed by the distant view camera at Yakushima (Fig. 1) (Japan Meteorological Agency, 2015). Its PDC flowed down from the summit area and reached a point ~3 km from the crater beyond the coastal line (Geshi et al., 2016). The 2015B eruption occurred during bad weather, so the height of the eruption column is unknown. However, information about the direction of the eruption cloud was obtained. The PDC current of the 2015B eruption with cloud cover around the summit was not observed by the distant view camera at station KEMN. Lapilli fall was observed ~9 km ENE from the summit, and the ash fall was distributed in the northern part of Yakushima and Tanegashima (Fig. 1) (Japan Meteorological Agency, 2015).

3. Seismic and infrasound observation

Table 1. Operation status of seismic and infrasound stations during the three eruptions

Station	Seismometer	Microphone	August 3, 2014	May 29, 2015	June 18, 2015
Around Shindake	Broadband Akashi V907 Short-period Akashi J21-3D	NA	Operated until the time of the eruption	Not operated	Not operated
KUCM	NA	Hakusan SI-103U (until Jan. 21, 2015) Hakusan SI-104	Operated	Operated	Operated
KEHT	Borehole Akashi JTS, natural period of 1 s	Aco 7144	Operated	Operated, but communication interrupted	Only vertical component operated
KER4	Short-period L4C-3D, natural period of 1 s	NA	Only vertical component operated	Only vertical component operated	Only vertical component operated
KCFV	Broadband Trillium 240	NA	Operated, but data not transmitted to SVRC	Operated	Not operated due to outage
KCNV	Broadband Trillium 240	NA	Operated, but data not transmitted to SVRC	Operated, but communication interrupted, and sensor tilted	Operated
KYKF	Broadband STS-2	NA	Operated	Operated	Operated

Sakurajima Volcano Observatory (currently Sakurajima Volcano Research Center (SVRC)) began continuous seismic observation at Kuchinoerabujima with a short-period three-component seismometer at 0.4 km west from Shindake crater in 1992. Three broadband seismometers were additionally installed around the crater in May 2002 by the observatory. Japan Meteorological Agency (JMA) also began seismic observations with one station near the crater in 1999 and added three stations around the crater in 2004. Both institutes also have seismic and infrasound stations on the flank of the volcano (Fig. 1 and Table 1). The National Research Institute for Earth Science and Disaster Resilience (NIED) was

constructing two stations (KCFV and KCNV) on the flank in 2014 and started retrieving broadband seismic data on May 22, sending data to JMA beginning on August 7. However, the installation of borehole seismometers and tiltmeters at the two NIED stations was halted by the 2014 eruption. Infrasound sensors are deployed at stations KUCM of SVRC, and two stations of JMA (at KEHT and near KUCM). We did not use these two JMA infrasound records, because the records of the 2015A eruption are saturated at KEHT and have abnormally small amplitude at the other site. The three institutes, SVRC, JMA, and NIED, have been sharing data since the 2014 eruption using the JDX net (Takano et al., 2008), a system for exchanging and distributing real-time seismic data over the JGN and SINET high-speed networks in Japan (Urushidani and Matsukata, 2008). KYKF station located at Yakushima (Fig. 1) is one of a nation-wide broadband seismic network (F-net) of stations (Okada et al., 2004).

The stations around the summit were destroyed due to the scattered ballistic blocks of the 2014 eruption (Geshi et al., 2016). The seismic waves excited by the eruption were obtained at the stations until the ballistic blocks bombarded the stations (Iguchi et al., 2017). Since the 2015A eruption, data transmissions from the stations on the flank have been frequently interrupted to SVRC due to outages at the settlements on Kuchinoerabujima by landslides and lahars. Table 1 shows a list of stations used in this study, indicating the models of the seismometers and infrasound microphones and the data retrieval status. There is no period when data from all stations are available for the 2014, 2015A, and 2015B eruptions. In this study, therefore, we use limited numbers of stations for analyzing the seismic and acoustic waves excited by the eruptions.

4. Characteristics of seismic and acoustic waves and estimation of duration of eruptions

We estimate the durations of the eruptions using the seismic and acoustic waves associated with the eruptions. We carefully investigated the characteristics of the waveforms from all available data of the stations as shown in Fig. 1 and Table 1. Figure 2 shows examples of the seismic and acoustic waveforms associated with the eruptions. The duration of an eruption is defined as follows: (1) The onset time of the infrasound signal excited by the eruption is measured. (2) The termination time of the infrasound signal is measured by judging whether the signal level is above the background noise. (3) The duration of the infrasound signal is equal to the time difference between the onset and termination times but is rounded off to the nearest 10 s. (4) The corresponding signal on a vertical component seismogram is also inspected using the same procedure as that for the infrasound signal. However, it is difficult to define the termination time of the seismic signal of the eruption because the seismogram is contaminated with the seismic events that occur beneath and around the volcano. For example, several small seismic events are seen before and after the infrasonic signal arrivals (see Fig. 2a). Therefore, we adopt the duration of the infrasound signal as the duration of the eruption. As a result, the durations are 50 s, 6 min, and 6 min for the 2014, 2015A, and 2015B eruptions, respectively (Fig. 2). The 6-min duration of the 2015A eruption is consistent with the witness report (Uhira and Toriyama, 2015), documenting that strong explosive activity of the 2015A eruption ended within 10 min, followed by a low and continuous emission of steam. The infrasound record of the 2014 eruption is very noisy due to microseism excited by Typhoon No. 12; therefore, the record is filtered in a pass-band greater than or equal to 0.5 Hz (Fig. 2b).

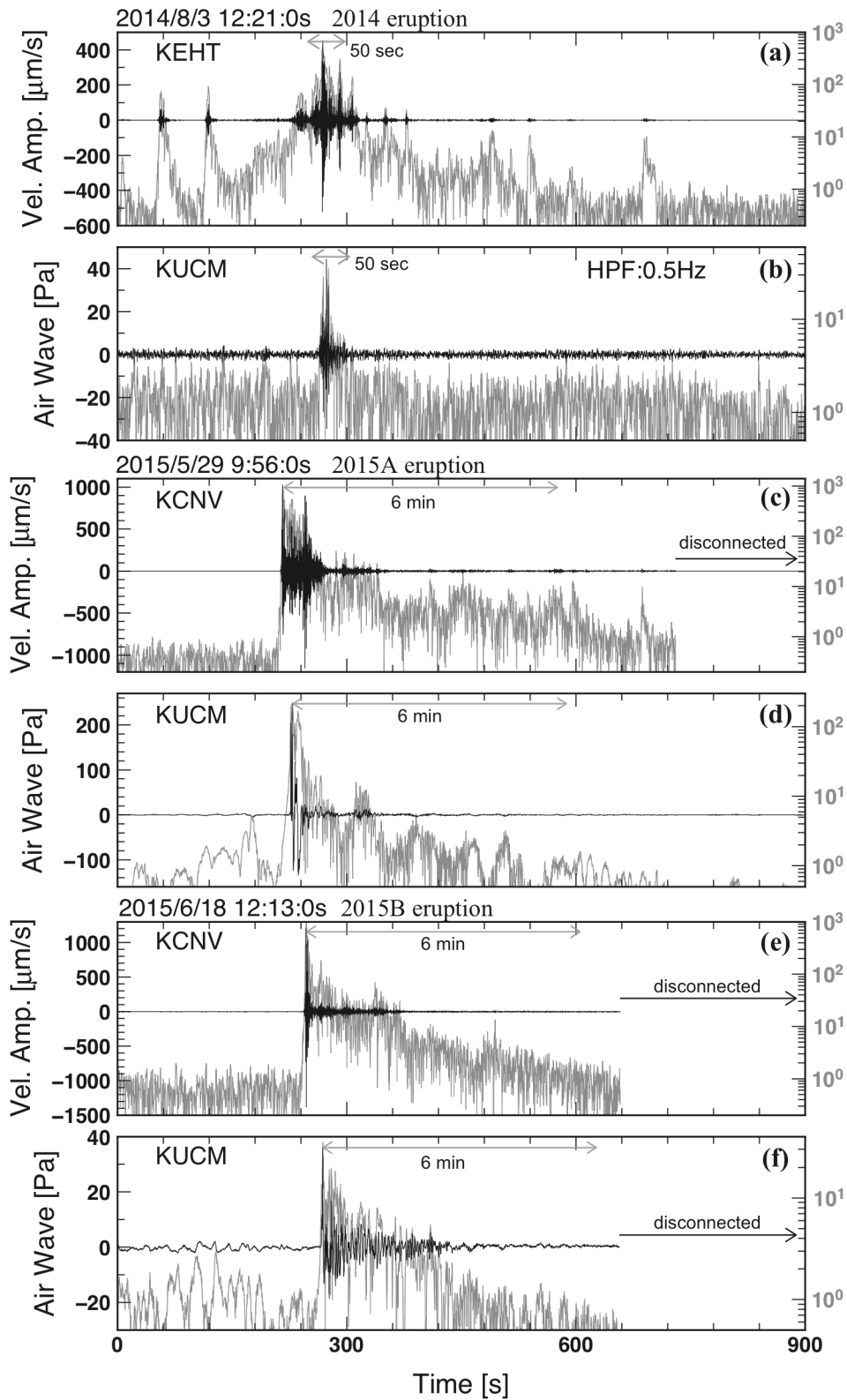


Fig.2. Comparison of short-period seismic and infrasound waveforms (black lines) and their envelope (gray lines) of the 2014 and 2015 eruptions. (a) (b) seismic and infrasound record of the 2014 eruption, respectively. (c) (d) seismic and infrasound record of the 2015A eruption, respectively. (e) (f) seismic and infrasound record of the 2015B eruption, respectively. All records are unfiltered, except for the infrasound record (b) of the 2014 eruption, which is filtered in a pass-band greater than or equal to 0.5 Hz. The envelopes are shown in log scale.

The overall shapes of the infrasound and seismic waveforms of the three eruptions are different, although the three eruptions are commonly categorized as phreatomagmatic eruptions (Geshi et al., 2016). Figure 3 shows the infrasound and vertical seismic records for the three eruptions. The infrasound record of the 2014 eruption is filtered in a pass-band greater than or equal to 0.5 Hz (Fig. 3a). The envelope of the infrasound and seismic waves is spindle-like for the 2014 eruption (Fig. 3a, d). This spindle-like shape was also found on the seismic signal associated with the 2014 phreatic eruption at Mt. Ontake (Kato et al., 2015). However, the shapes of the 2015A and 2015B eruptions are different from that of the 2014 eruption and have an impulsive large first arrival phase, which is followed by long-tail small amplitude arrival phases (Fig. 3b, c, e, f). This pattern is found on both the infrasound and seismic waveforms and is also found on small Vulcanian eruptions (e.g., Fee and Matoza, 2013; Yamada et al., 2016). The characteristics of the waveforms of the 2015 eruptions are somewhat different, as the acoustic wave of the 2015A eruption has clear secondary impulsive and minor third phases about 2 s and 5 s after the first impulsive phase, respectively (Arrows in Fig. 3b). The first, secondary and third phases of the infrasound record correspond to those of the seismic record, but the first and secondary seismic phases overlap each other and the third is obscure (Fig. 3e). The maximum amplitudes of the infrasound signals of the three eruptions are different, while there is no significant difference between those of the seismic signals (Fig. 3d, e, f). The infrasound maximum amplitude of the 2015A eruption is 230 Pa, and the minimum is -110 Pa (Fig. 3b). This amplitude variation is much larger than those of the 2014 and 2015B eruptions (Fig. 3a, c).

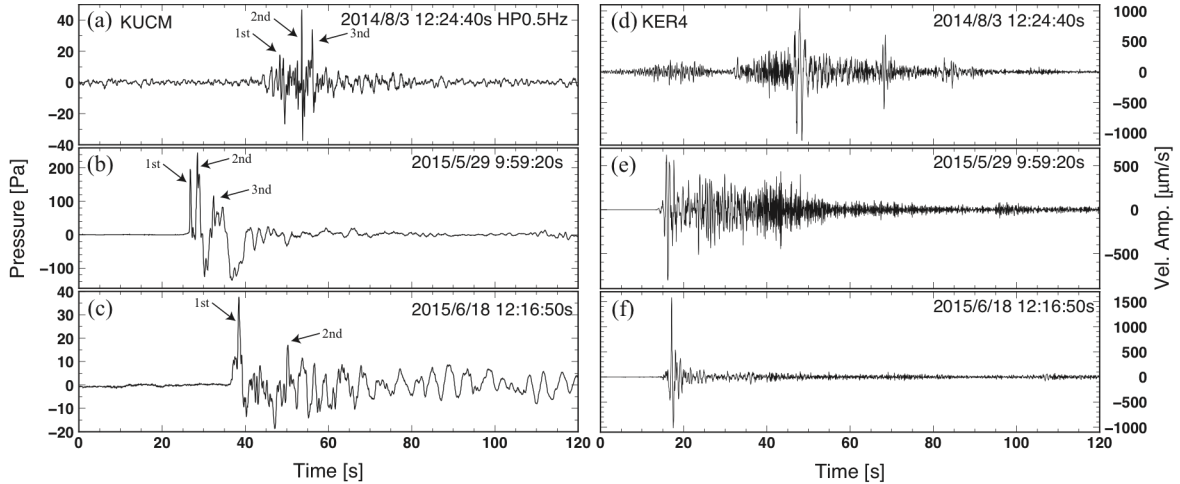


Fig.3. Comparison of short-period seismic and infrasound waveforms of the 2014 and 2015 eruptions. (a), (b) and (c) are infrasound records of the 2014, 2015A and 2015B eruptions, respectively. (d), (e) and (f) are vertical seismic records of the 2014, 2015A and 2015B eruptions, respectively. All records are unfiltered, except for the infrasound record (a) of the 2014 eruption, which is filtered in a pass-band greater than or equal to 0.5 Hz. Note that the arrival time differences between seismic and infrasound waves are about 5, 10 and 20 s for the 2014, 2015A and 2015B eruptions, respectively.

Note that the arrival time difference between the seismic and infrasound signals is about 5 s for the 2014 eruption while those for 2015A and 2015B are about 10 and 20 s, respectively (Fig. 3). Comparing arrival times of seismic waves of distant regional earthquakes for the stations in the island, we did not find any significant time differences between them and any timing problem due to GPS time correction failure. The arrival time difference of the infrasound signals between KUCM and KEHT was 2.7, 0.9 and 1.3 s for the 2014, 2015A and 2015B eruptions, respectively. Considering the sound speed of 0.34 km/s and station distances from the crater, the arrival time difference was estimated to be 1.4 s. The arrival time difference is partially explained by the difference of station distances between KUCM and KEHT. However, it is impossible to explain the change of the time difference between the seismic and infrasound signals from 5 to 20 s for the 2014 and 2015 eruptions. Although detailed discussions of the change are beyond the scope of this paper, the change of the time difference could reflect a change

in physical properties and/or a migration of the seismic source in the conduit, as suggested for explosions at Stromboli (Ripepe et al., 2001).

5. Seismic and acoustic energy

Seismic energy is calculated from the time integral of the squared velocity of the seismogram. Assuming an isotropic source at the top of a homogeneous half space, the seismic energy in terms of body waves is shown by Johnson and Aster (2005) as:

$$E_{seismic} = 2\pi r^2 \rho_{earth} c_{earth} \frac{1}{A} \int S^2 U(t)^2 dt \quad (1)$$

where r is the source station distance, ρ_{earth} is the density of the medium, c_{earth} is the body wave propagation speed, S is the site response, $U(t)$ is the seismic velocity amplitude, and t is the time. Here S is assumed to be 1 because the site effect is not evaluated in this study. The term A is the attenuation factor of seismic energy defined by:

$$A(r) = e^{-2\pi f r / (c_{earth} Q)} \quad (2)$$

where f is the predominant frequency of the seismic wave, and Q is the quality factor.

Low-amplitude infrasound propagates with an energy density that is proportional to the square of the excess pressure (ΔP) divided by the air density (ρ_{atmos}) and sound speed (c_{atmos}). Assuming isotropic radiation, as from a point source monopole, the acoustic energy is shown by Johnson (2003) and Johnson and Aster (2005) to be:

$$E_{acoustic} = \frac{2\pi r^2}{\rho_{atmos} c_{atmos}} \int \Delta P(t)^2 dt \quad (3)$$

Both seismic and acoustic signals are filtered with a two-pole Butterworth band-pass filter of 0.5–12 Hz. This pass-band is the same as that used for seismic waves excited by Strombolian eruptions at Karmisky and Erebus Volcanoes (Johnson and Aster, 2005) and Vulcanian eruptions of Popocatepetl Volcano (Arámbula-Mendoza et al., 2013). Here, we assume the parameters as $\rho_{earth} = 2000 \text{ kg/m}^3$, $c_{atmos} = 2.5 \text{ km/s}$, $f = 6 \text{ Hz}$, which is the center of the pass-band, and $Q = 65$ for the seismic energy, and as $\rho_{atmos} = 1.2 \text{ kg/m}^3$, $c_{atmos} = 0.34 \text{ km/s}$ for the acoustic energy. The seismic energy can depend on the parameters; therefore, we will discuss the dependency later. To characterize the acoustic energy corresponding to the eruptions, we integrate over a time window spanning the entire duration of the acoustic transient. The integral is calculated from the signal onset until the time when both seismic and acoustic amplitude have decayed to background levels. The seismic energy for each component of the seismogram is calculated, and we sum the three-components of the seismic energy to obtain the three-component seismic energy.

Figure 4 shows the acoustic and seismic energy rate (energy per second) and their cumulative energy (total acoustic and seismic energy) for the three eruptions. For the 2014 eruption, there are three acoustic energy arrivals and the middle one is the largest (Fig. 4a top), reflecting the spindle-like shape waveform (Fig. 3a). Two distinct seismic energy arrivals are found; the first one corresponds to the acoustic energy arrivals, but the second one does not (Fig. 4a middle lower). For the 2015A eruption, two distinct acoustic energy arrivals exist and correspond to two distinct seismic energy arrivals (Fig. 4b top and middle lower). However, there are minor seismic energy arrivals following the distinct arrivals (Fig. 4b middle lower), while this is not the case for the acoustic energy (Fig. 4b top). For the 2015B eruption, one distinct energy arrival commonly exists, and the arrival is followed by minor energy arrivals for both seismic and acoustic energies. Note that the arrival time difference between the acoustic and seismic energy peaks is about 5 s for the 2014 eruption while those for 2015A and 2015B are about 10 and 20 s, as shown previously in Fig. 3. It is difficult to explain the time differences by the travel times of seismic waves. Because the horizontal distances from Shindake crater to the stations are different and

are 2.35 km, 1.5 km, and 1.6 km for stations KEHT, KCFV, and KCNV, respectively, the time difference of the travel times is less than 0.3 s.

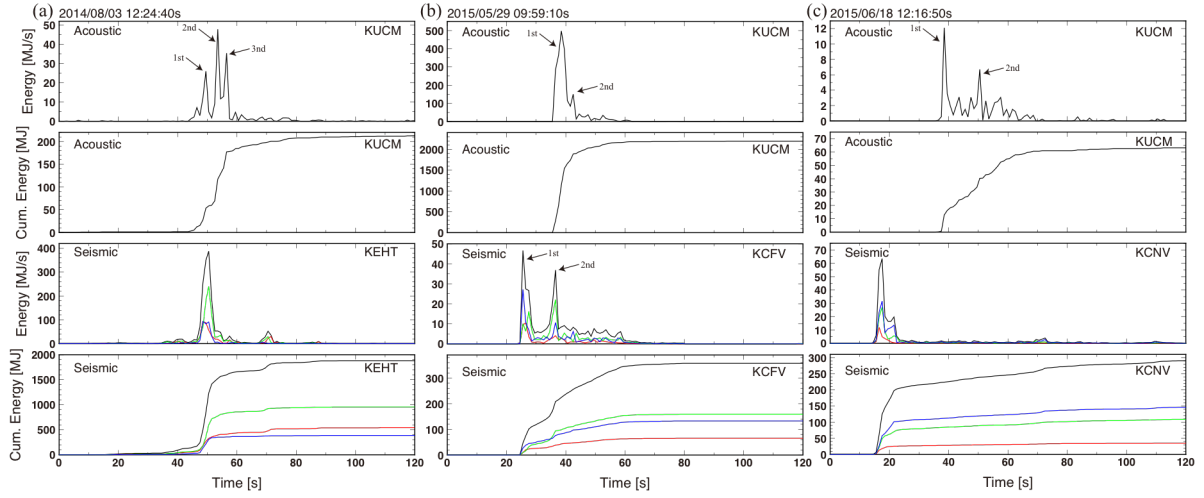


Fig.4. Sismic and acoustic and cumulative seismic and acoustic energies for the (a) 2014, (b) 2015A, and (c) 2015B eruptions. For each eruption, acoustic energy, cumulative acoustic energy, seismic energy, and cumulative seismic energy are shown from the top to the bottom. For the seismic energy, red, green, and blue lines show vertical, north-south and east-west components, and black lines show the total of the three components.

The total cumulative acoustic and seismic energies are measured at flat levels of the cumulative energy flux (Fig. 4 middle, upper, and bottom). The total cumulative acoustic energy is 0.212 GJ, 2.20 GJ, and 0.0648 GJ for the 2014, 2015A, and 2015B eruptions, respectively. The total cumulative seismic energy is 1.88 GJ, 0.358 GJ, and 0.296 GJ for the 2014, 2015A, and 2015B eruptions, respectively. The sum of both total cumulative seismic energies is 2.09 GJ, 2.55 GJ, and 0.361 GJ for the 2014, 2015A, and 2015B eruptions, respectively.

The volcanic acoustic-seismic ratio (VASR) is the ratio of the acoustic to seismic energies (Johnson and Aster, 2005), $\eta = E_{acoustic}/E_{seismic}$. The VASR is a non-dimensional parameter, which may be related to different explosion mechanisms, and their physical interpretations may be useful in comparing processes at an individual or various volcanoes (Johnson and Aster, 2005). The VASR values for the 2014, 2015A, and 2015B eruptions are 0.11, 6.1, and 0.22, respectively. Figure 5 shows comparisons between the total cumulative acoustic and seismic energies, and the slope corresponds to VASR. The colored hatched regions correspond to the seismic and acoustic energies for Strombolian eruptions at Karymsky and Erebus (Johnson and Aster, 2005), and the pluses correspond to those for Vulcanian eruptions at Popocatépetl, Mexico (Arámbula-Mendoza et al., 2013). Because Vulcanian eruptions are more energetic than Strombolian eruptions, the seismic and acoustic energies of the Vulcanian eruptions are greater than those of the Strombolian eruptions. The data points for the 2014 and 2015 eruptions at Kuchinoerabujima are located in the region of the Vulcanian eruptions at Popocatépetl.

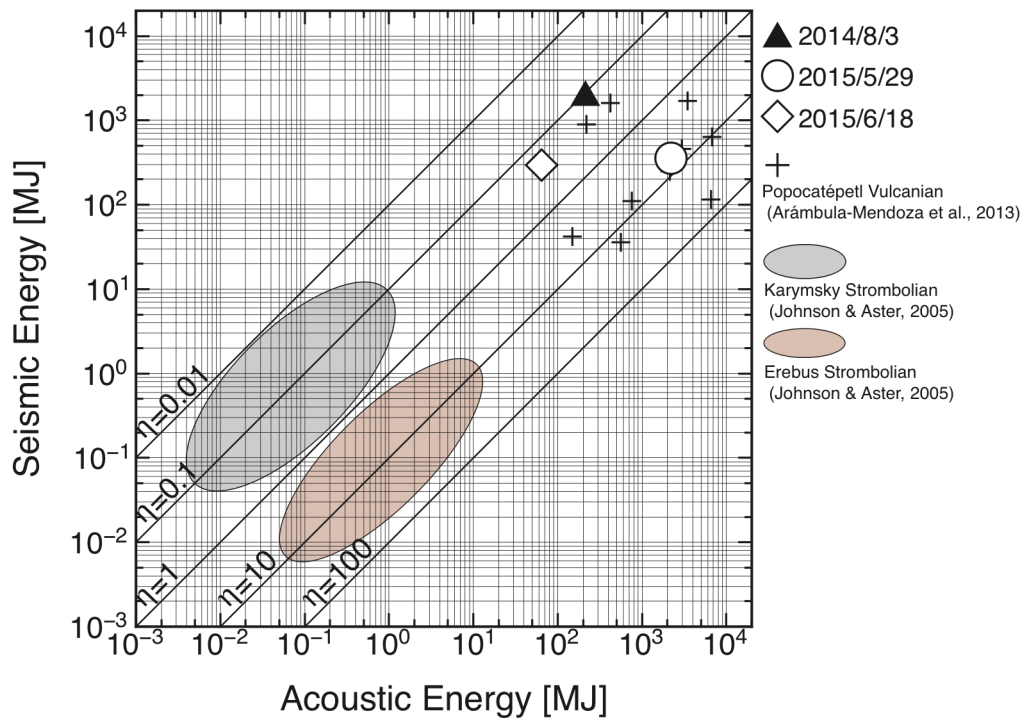


Fig.5. Comparison between total seismic and acoustic energies for the (a) 2014, (b) 2015A, and (c) 2015B eruptions. Each inclined line has a constant volcanic acoustic-seismic ratio (VASR). The black triangle, open circle and open diamond correspond to the 2014, 2015A, and 2015B eruptions, respectively. The colored hatched oval regions roughly trace the total seismic and acoustic energies for explosive eruptions at other volcanoes. The gray and brown regions show Strombolian eruptions at Karymsky, Russia, and Erebus, Antarctica (Johnson and Aster, 2005). The pluses show moderate Vulcanian eruptions at Popocatépetl, Mexico (Arámbula-Mendoza et al., 2013).

6. Single force analysis

In this section, a single force analysis is conducted for comparison of the size of eruptions. Here we analyze the 2015A and 2015B eruptions, because the 2014 eruption formed several fissures around Shindake crater as described previously (Geshi et al., 2016) and its source mechanisms might not be explained by a single force. When the 2015A eruption occurred on May 29, 2015, two broadband seismic stations, KCFV and KCNV, were operating (Table 1). However, in this study, the broadband seismograms of KCNV of the 2015A eruption were not used for the analysis because the tilt step response of a broadband seismometer was shown in the record, as shown in a comparable experiment between a tiltmeter and a broadband seismometer (Aoyama, 2008). The tilt step may be generated by fallen ballistic blocks of the eruption around KCNV station. When the 2015B eruption occurred on June 18, 2015, only one broadband station (KCNV) operated (Table 1).

The seismic wave excited by the 2015A eruption is dominant in the frequency band of 0.1–1 Hz, and its dominant frequency is 0.8 Hz, which is evaluated by consulting its power spectrum of the broadband record at KCFV station. To understand the nature of the first arrival phase of the seismic record of the 2015A eruption, we plot the particle motion for the first arrival phase of the seismic record in Fig. 6. To avoid the influence of high-frequency noise and low-frequency fluctuation, the records of vertical, radial, and transverse components were band-pass filtered between 0.1–1 Hz. We find that the radial linear motion of particles in the radial-transverse plane and the retrograde motion of particles from well-expressed ellipses in the vertical-radial plane are characteristics of Rayleigh waves. By using the same band-pass filter, we also find that the first arrival phase of the seismic record of the 2015B eruption has characteristics of Rayleigh waves. We focus on the first arrival phases and do not discuss the high-frequency later arrival phases for the 2015A and 2015B eruptions.

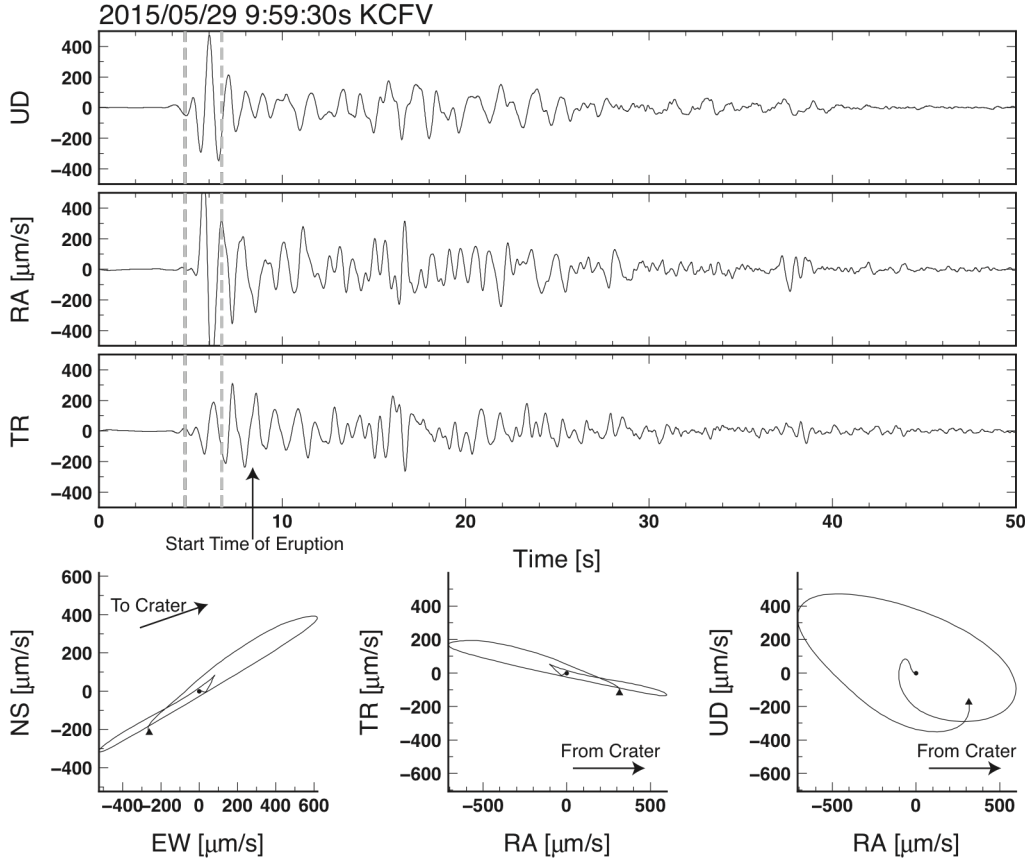


Fig.6. Waveforms and particle motions recorded at KCFV station filtered in the 0.1 - 1 Hz band for the beginning of the 2015A eruption at 9:59 JST on May 29, 2015. (a) Filtered vertical, radial, and transverse waveforms. The radial direction is from Shindake crater to the station; the transverse direction is perpendicular to the radial direction and clockwise. Particle motions of the signals within the windows marked by vertical gray dashed lines are plotted in (b). Particle trajectories start at the circles and end at the triangles. (b) On the left panel, the north-south motion is plotted versus the east-west motion. The middle and right panels, where transverse and vertical motions, respectively, are plotted against radial motion, display retrograde motion of Rayleigh waves.

The Rayleigh nature of the seismic wave representing the first arrival phase allows us to use the methodology of modeling the first arrival phase as a Lamb's pulse with an estimation of the counter force of the eruption (Kanamori and Given, 1983). This nature is also reported for explosion earthquakes at Mt. Asama (Nishimura and Hamaguchi, 1993; Nishimura and Uchida, 2005), Mt. Tokachi (Nishimura, 1995), Mt. Colima (Zobin et al., 2006a, 2006b), and Mt. Popocatepetl (Cruz-Atienza et al., 2001). We estimate the amount of force at the eruption source and the time width of the force by comparing the three-component broadband seismograms at KCFV and KCVN to their theoretical ones for the 2015A and 2015B eruptions, respectively. The epicenter of the force is fixed at the center of Shindake crater, but the depth of the force is variable and grid-searched by the following procedure.

Table 2. One-dimensional structure of densities, P - and S -wave velocities, and quality factors. The structure as shown with values in parentheses at Layers 1 and 2 is used for station KCVN.

Layer	Density (g/cm^3)	V_P (km/s)	V_S (km/s)	Q_P	Q_S	Thickness (km)
1	1.91 (2.36)	2.00 (3.80)	0.61 (2.11)	50 (100)	30 (50)	0.2
2	2.25 (2.36)	3.10 (3.80)	1.50 (2.11)	80 (100)	40 (50)	0.2
3	2.36	3.80	2.11	100	50	0.2
4	2.39	4.00	2.28	100	50	0.4
5	2.43	4.30	2.52	100	50	0.5
6	2.48	4.60	2.74	150	80	0.5
7	2.53	5.00	3.01	150	80	0.5
8	2.58	5.30	3.19	200	100	1.5
9	2.70	5.96	3.52	220	100	2.0
10	2.72	6.02	3.56	250	110	2.0
11	2.74	6.10	3.60	250	110	2.0
12	2.76	6.18	3.63	330	150	2.0

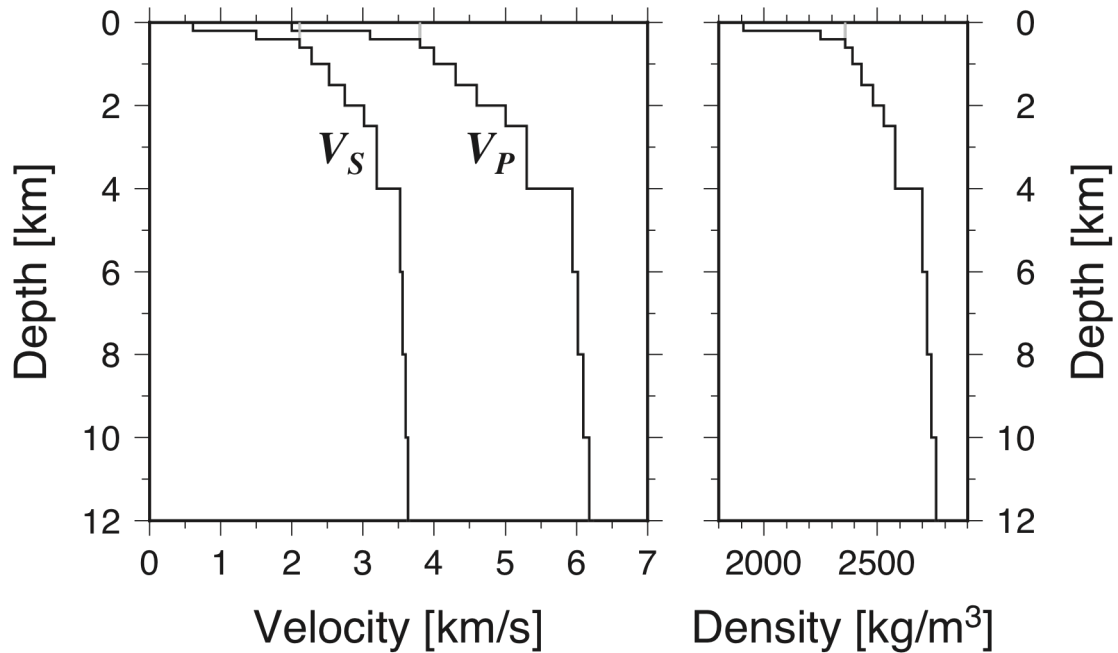


Fig.7. Velocity and density structures used for calculation of synthetic waveforms for KCFV (black lines) and KCVN (grey lines at a depth of 0–0.4 km corresponding to Layers 1 and 2, see **Table 2**).

We calculated the time domain synthetic seismograms excited by a single vertical pulse of counter force F originating at depth D beneath the crater and recorded at distances of 1.5 km and 1.65 km, between the crater and KCFV and KCVN stations, respectively (Fig. 1). Depth $D = 0$ km is defined to be the heights (0.16 km and 0.18 km above sea level) of station KCFV and KCVN, respectively. We use the discrete wavenumber method (Bouchon, 1979, 1981) and the reflection and transmission coefficient matrices (Kennett and Kerry, 1979) for calculating the synthetic waves using a flat layered one-dimensional (1-D) structure (Table 2 and Fig. 7). The 1-D V_p structure is extracted from results of the 2004 active source experiment (Iguchi et al., 2005). The 1-D V_s and density structure are converted band-pass filtered between 0.1–1 Hz. The squared error of the vertical and radial components between the observed and synthetic waveforms is calculated for a 2-s time window (number of samples: $N_s = 41$) that contains the first arrival phase. Note that a transverse component is not excited by the synthetic calculation, because the counter source is a vertical direction force and axially symmetric, and the 1-D structure is assumed. Squared error E follows the definition by Ohminato et al. (1998) for the single station case as follows:

$$E = \frac{\sum_{n=1}^2 \sum_{p=1}^{N_s} (u_n^O(p\Delta t) - u_n^S(p\Delta t))^2}{\sum_{n=1}^2 \sum_{p=1}^{N_s} (u_n^O(p\Delta t))^2} \quad (4)$$

where $u_n^O(p\Delta t)$ represents the p -th sample of the n -th data component and $u_n^S(p\Delta t)$ represents the p -th sample of the n -th component of the synthetic waveforms. We change the three parameters of depth D , pulse width τ , and amount of force F to seek the minimum of squared error E . Depth D varies from 0.01 to 0.25 km with an interval of 0.01 km, from 0.25 to 0.4 km with an interval of 0.05 km, and from 0.4 to 1 km with an interval of 0.1 km. Pulse width τ varies from 0.2 to 2.0 s with an interval of 0.1 s. Force F varies at 5×10^9 , 1×10^{10} , 1.5×10^{10} , 2×10^{10} , 5×10^{10} , and 1×10^{11} N. Finally, we find the best-fit model with the minimum squared error of $E = 0.546$ and $E = 0.469$ for the 2015A and 2015B eruptions, respectively. For the 2015A eruption, the best-fit parameters of D , τ , and F are 0.19 km, 0.9 s, and 1.5×10^{10} N, respectively. For the 2015B eruption, parameters D , τ , and F are 0.16 km, 1.6 s, and 5×10^{10} N, respectively. Taking into account the height of the station, source depths D for the 2015A and 2015B eruptions are 30 m and 0 m below sea level, respectively. Figure 8 shows a comparison between the observed and synthetic waveforms, which are band-pass filtered between 0.1–1 Hz. The synthetic waveforms are calculated for the best-fit parameters. The good fit between the observed and synthetic waveforms for vertical and radial components indicates that the observed features are fairly

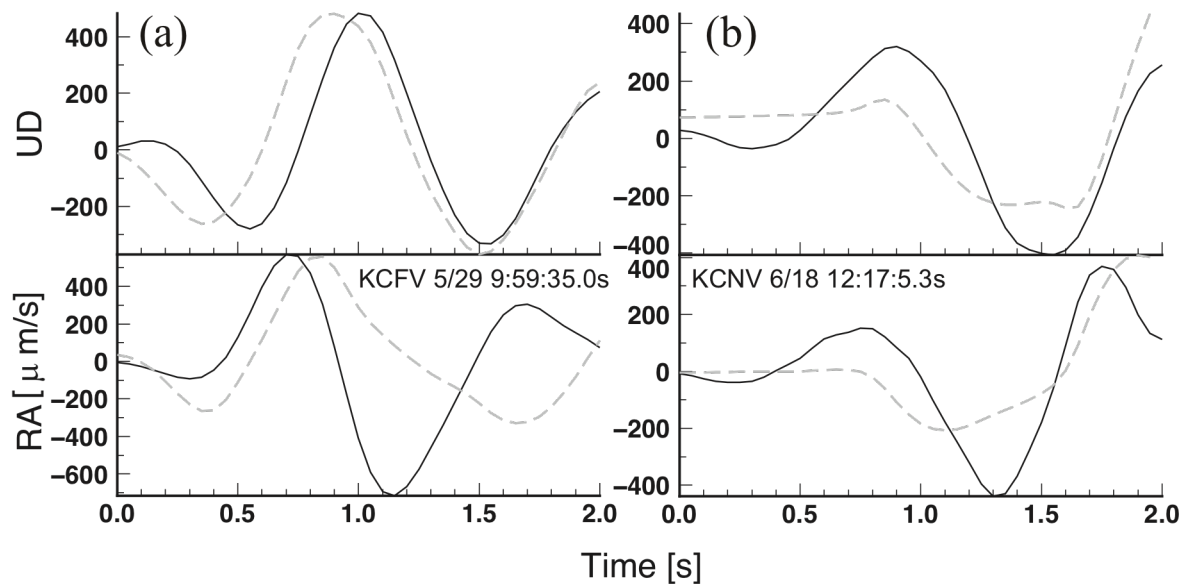


Fig.8. Waveform matches obtained by the single force analysis. (a) Station KCFV of the 2015A eruption. (b) Station KCVN of the 2015B eruption. Solid black and dashed gray lines represent the observed and best-fit synthetic seismograms, respectively.

well reproduced by the synthetic waveforms calculated for the best-fit solutions of both eruptions. However, discrepancies in the waveform fits may occur because the source may not be simply represented by a vertical single force or unknown structure, and a topographic effect may exist. The unmolded source, unknown structure, and topography will be taken into account in future waveform fittings, which are beyond the scope of this study.

In order to verify the obtained best-fit parameters, we compare the observed and synthetic waveforms for KYKF station. The observed waveforms at KYKF are corrected with the response of the STS-2 broadband seismometer and band-pass filtered between 4 and 40 s to reduce long-period microseisms excited by ocean waves. Since the velocity structure between Kuchinoerabujima and Yakushima Island is unknown, it is difficult to match observed and synthetic seismograms of KYKF station for the eruption earthquakes. Therefore, we just compare the amplitudes between the observed and synthetic waves for the 2015A eruption. We do not compare the amplitudes for the 2015B eruption, because the long-period (>10 s) seismic signals excited by the 2014B eruption are not clear at KYKF station (Matsuzawa et al., 2016). The amplitudes of the radial component of the response-corrected and filtered seismograms are about $\pm 1.5 \mu\text{m/s}$ for the first arrival phase of the 2015A eruption. For the synthetic calculation, depth D , pulse width τ , and force F are fixed to 0.19 km, 0.9 s and 1.5×10^{10} N, respectively. The amplitude of the filtered synthetic radial waveform is $\pm 1.9 \mu\text{m/s}$. Since the difference between the observed and synthetic seismic amplitudes is not significant, the best-fit parameters are verified by the records from KYKF station.

7. Discussion

Estimation of seismic energy can depend on the assumed parameters. Here we evaluate the dependency of quality factor Q and body wave propagation speed c_{earth} . For volcanic regions, quality factor Q varies from 10 to 100 at shallow depths, which is less than 5 km (e.g., Clawson et al., 1989). Johnson and Aster (2005) and Arámbula-Mendoza et al. (2013) adopted the quality factor value of $Q = 10$, which is the lowest value of Q . To evaluate the dependency, we calculate the seismic energy by using several sets of quality factors and speeds as shown in Table 3. The seismic signals are filtered with the same band-pass filter of 0.5–12 Hz. Seismic energy is calculated for the case of a body wave propagation speed $c_{earth} = 1.4$ km/s corresponding to the S -wave velocity at shallow layers (Layers 1 and 2 shown in Table 2), although the original energy calculation is performed using a wave-speed value corresponding to the P -wave velocity at the shallow layers. The dependency of the propagation speed of the seismic wave type is not significant compared to the dependency of the quality factor. The largest difference exists between the quality factors of $Q = 10$ and others. For example, there is about 10 times difference between Case 1 and 2. Therefore, the seismic energy might be an overestimate for the case of $Q = 10$.

Table 3. Comparison between cumulative seismic energies and assumed parameters.

Case	Quality factor	c_{earth} (km/s)	Cumulative seismic energy (GJ)		
			2014	2015A	2015B
1	10	1.4	19.0	1.27	1.15
2	65	1.4	1.31	0.230	0.186
3	100	1.4	1.10	0.206	0.166
4	10	2.5	8.43	0.931	0.800
5	65	2.5	1.88	0.358	0.296
6	100	2.5	1.71	0.336	0.270

The 2014, 2015A, and 2015B eruptions commonly produced pyroclastic materials consisting of a mixture of various types of rock fragments (Geshi et al., 2016). These eruptions blew up the hydrothermally-altered materials and also a part of the intruded magma, which is suggested by precursory phenomena (Iguchi et al., 2017). The volcanic ashes are mainly composed of the hydrothermally-altered rock fragments. The lapilli consist of both fresh and crystalline rock fragments and hydrothermally-altered lava fragments (Geshi et al., 2016). However, the difference between the 2014 and 2015 eruptions is the formation of fissures. The 2014 eruption formed two eruption fissures with north-south and ENE-WSW trends, which traced the eruption fissures formed in the 1931 eruption (Geshi et al., 2016). The 2015A and 2015B eruptions occurred at the bottom of Shindake crater. Although the depth of Shindake crater increased after the eruptions, there was no significant change in the horizontal outline of the crater, and the fractures formed by the 2014 eruption remained after the 2015 eruptions (Geshi et al., 2016).

The duration and shape of the seismic and acoustic waveforms of the 2014 eruption are quite different from those of the 2015A and 2015B eruptions. The difference may be related to the formation of fractures in Shindake crater. As described previously, the duration of the 2014 eruption was 50 s, much shorter than the 6 min durations of the 2015 eruptions (Fig. 2). The seismic and acoustic waveforms of the 2014 eruption have a spindle-like shape (Fig. 3), suggesting that the eruption was initially weak, gradually became violent, and then stopped. The eruption energy of the 2014 eruption was largely used for forming new fractures and was also converted to seismic energy during the formation of the fractures. The remainder of the energy during and after the formation was converted to acoustic energy, resulting in the low VASR of 0.47 (Fig. 5). The seismic energies for the 2015 eruptions were lower than those for the 2014 eruption, as no new fissures were formed in the crater by the 2015 eruptions. The seismic energy was roughly the same for the 2015A and 2015B eruptions, while the acoustic energy of the 2015A eruption was over 30 times larger than that of the 2015B eruption, resulting in the high VASR value for the 2015A eruption (Figs. 4 and 5). Although both the 2015A and 2015B eruptions had explosive eruption natures, the strength of the capped conduit (ballistics plug) below the crater before the occurrence of the eruptions may have been different for both eruptions, as the strength of the 2015A eruption was much larger than that of the 2015B eruption as seen in the difference of the acoustic energy and maximum amplitudes (Figs. 3 and 4).

In this study, we did not apply the single force method to the 2014 eruption, because we believe that the source mechanism of the 2014 eruption earthquake was not simply expressed by a single force and possibly had shear faulting components. As described previously, the 2014 eruption formed fissures, which may have been promoted by the structural instability of the edifice of Shindake (Geshi et al., 2016). Several eruption fissures had been formed by the previous 1931, 1945, and 1980 eruptions and were promoted by the westward sliding of the edifice of Shindake (Geshi et al., 2016). This westward sliding may be caused by an east-west extensional stress, which is supported by the normal fault type mechanisms with the WNW-ESE extension of the shallow volcano-tectonic (VT) earthquakes (Triastuty et al., 2009). The source mechanisms of the 2014 eruption earthquake will be investigated considering the normal faulting component in a future study.

As seen in the movie from the camera at KEMN station, the 2015A eruption initially ejected vertically and then ejected an inclined blast in the NWN direction 5 s afterward. As seen in Fig. 6, the initial arrival phase corresponds to the initial vertical ejection, but the arrival phase that corresponds to the inclined blast is not clear. Matsuzawa et al. (2016) elucidated the vertical component of the single force and the horizontal force component that is directed in a north-south direction and suggested that this horizontal force corresponds to the blast. Therefore, the inclined counter force will be applied in a future study as it is beyond the scope of this study. Matsuzawa et al. (2016) point out that the peak amplitudes of the horizontal single force are similar to that of the vertical force, and, in addition, the initial phase of the vertical force precedes that of the horizontal by several seconds. In our case, only the initial phase is modeled. The discrepancy between the observed and synthetic waveforms for the vertical and radial components (Fig. 8) may be reduced by the waveform modeling taking into account the more complex seismic sources, including an inclined force and or moment tensor and also the topographic effects of the volcano edifice (e.g., Ohminato and Chouet, 1997).

Seismic waves excited by explosive eruptions have frequently been modeled by the waveform inversion technique assuming a counter downward force (e.g., Kanamori et al., 1984; Nishimura and Hamaguchi, 1993; Ohminato et al., 2006). As described previously, the seismic waves excited by the

2015 eruptions are also modeled by the counter force model. Nishimura and Hamaguchi (1993) proposed the relationship between the counter forces and pulse width using the following scaling law:

$$\log F = 2 \log \tau + 2 \log(v/3) + \log P + \log \pi \quad (5)$$

where v is the initial particle velocity of the flow of the ejected materials of an eruption and P is the initial pressure in a conduit before the eruption. The lines for the scaling law are shown for initial pressure $P = 0.1, 1, \text{ and } 10 \text{ MPa}$ in Fig. 9. The counter forces and the pulse widths of the single forces for the 2015A and 2015B eruptions are shown on the scaling line for the pressure of 6 MPa (Fig. 9). We compare the results of the 2015A and 2015B eruptions with the results of several volcanoes around the world (Fig. 9). The counter force and pulse width for the 2015A eruption are the same as that of the Vulcanian eruptions of Tokachi-dake, Japan in 1989 (Nishimura, 1995; Kato et al., 2002). The counter force and pulse width of the 2015B eruption are similar to those of the Vulcanian eruptions of Mt. Asama in 1983 and 2004 (Nishimura and Uchida 2005; Ohminato et al., 2006) and Mt. Colima in 2003 (Zobin et al., 2006a), 2004 and 2005 (Zobin et al., 2006b). The points of the counter forces and pulse widths for the 2015 eruptions are located between the scaling lines for the pressure of 0.1–10 MPa (Fig. 9). The 2015A and 2015B eruptions lie in the higher-pressure regime, suggesting a higher internal pressure in the conduit below the crater before the eruption occurred.

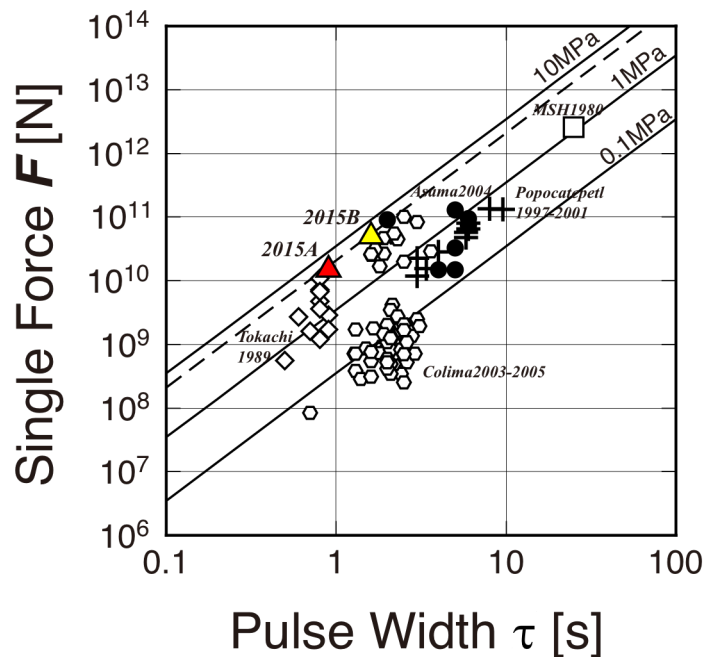


Fig.9. Relationship between the counter force of eruption F and the pulse width of single force τ for the explosion earthquakes for a group of volcanoes of the world. The relationships between F and τ for the 2015A and 2015B eruptions of Kuchinoerabujima are shown by red and yellow triangles, respectively. The data for other earthquakes are shown for Colima in 2003 (Zobin et al., 2006a), 2004 and 2005 (Zobin et al., 2006b) as open hexagons, for Tokachi in 1989 (Nishimura, 1995; Kato et al., 2002) as open diamonds, for Asama in 1983 (Nishimura and Hamaguchi, 1993) and 2004 (Nishimura and Uchida, 2005; Ohminato et al., 2006) as black circles, for Popocatepetl (Cruz-Atienza et al., 2001) as black crosses, and for Mount St. Helens in 1980 (Kanamori et al., 1984) as an open square. The solid lines of scaling for three initial internal pressures of 0.1, 1, and 10 MPa proposed by Nishimura and Hamaguchi (1993) are shown. The dashed line shows the scaling line for the pressure of 6 MPa.

Geshi et al. (2016) analyzed non-altered grains in the volcanic ash from the 2014 and 2015 eruptions and found that fresh glassy grains exist, and the water content in the glass is 1.2–1.6 wt.%.

The presence of silica minerals in the grains suggests that the crystallization occurred at a low-pressure condition of less than 10 MPa, and the water contents correspond to the water solubility in a rhyolitic melt at 10–20 MPa (Geshi et al., 2016). This pressure corresponds to the lithostatic pressure at a depth of ~0.5–1 km, assuming the crustal density as 2000 kg/m³. The pressure corresponds to the pressure of 6 MPa estimated by the single force analysis of the seismic waves. The source depths of the 2015A and 2015B eruptions estimated by the single force analysis are 30 m and 0 m below sea level, respectively, roughly corresponding to the lithostatic pressure depth and to the depth of 0–100 m above sea level of the aquifer below Shindake that is suggested by the audio-frequency magneto-telluric survey (Kanda et al., 2010). Therefore, we interpreted that a magma head reached the aquifer below Shindake crater, water in the aquifer suddenly vaporized and then phreatomagmatic eruptions occurred.

Following the method of Prejean and Brodsky (2011), we estimate the mass discharge rate from the amount of the estimated single force. Vertical force F on the Earth can be related to mass discharge rate \dot{M} and volumetric discharge rate q using a momentum balance following Brodsky et al. (1999):

$$F = \dot{M}v = q\rho v \quad (6)$$

where v is the velocity of material discharging from the vent and ρ is the dense rock equivalent (DRE) density. Following Prejean and Brodsky (2011), we assume the vent exit speeds (v) to be 100–250 m/s. Therefore, we obtain the mass discharge rate \dot{M} of $0.6\text{--}1.5 \times 10^8$ kg/s using the estimated vertical force and Eq. (6) for the 2015A eruption. We do not discuss the 2015B eruption, because its column height was not measured due to bad weather. If DRE density ρ is 2500 kg/m³, volumetric discharge rate q is $2.4\text{--}6 \times 10^4$ m³/s. Following the equation of Mastin et al. (2009), the empirical relationship between the maximum column height in km above the vent and volumetric discharge rate q in m³/s is expressed as

$$H = 2q^{0.241}. \quad (7)$$

Using the volumetric discharge rate and Eq. (7), we obtain the maximum column height as 23–28 km from the vent, which is much higher than the observed column height of 9 km. The significant discrepancy between the estimated maximum column height and the observed one partially comes from suppression of the rising up of the eruption column due to a strong west-northwesterly wind of 14 m/s blowing over Kuchinoerabujima at an altitude of 7.5 km (Tanaka and Iguchi, 2016).

We do not estimate the amount of ejected materials from the eruptions using the seismic and acoustic energies in this study. Systematic analyses of the seismic and acoustic energies and the force of the seismic waves for the eruptions need to be conducted along with ash sampling surveys and remote sensing to evaluate the amount of the ejected materials. A new relationship between the energies and the amount of the ejected materials will be established in future studies.

8. Conclusions

As a limited number of stations were available for the analysis, we estimated the seismic and acoustic energies and durations of the eruptions. The durations of the eruptions were 50 s, 6 min, and 6 min for the 2014, 2015A, and 2015B eruptions, respectively. Although the ejected materials of the 2014 and 2015 eruptions were of phreatomagmatic origins, as suggested by geological surveys, the characteristics of the seismic and acoustic waveforms were different. The seismic and acoustic waveforms of the 2014 eruption were expressed by spindle shapes, suggesting that the eruption was initially weak and gradually became violent; while the waveforms of the 2015A and 2015B eruptions were expressed by shapes similar to a typical explosive eruption. The seismic and acoustic energies of the 2014 eruption were 1.88 GJ and 0.21 GJ, respectively. The seismic and acoustic energies of the 2015A eruption were 0.36 GJ and 2.2 GJ, respectively, and the seismic and acoustic energies of the 2015B eruption were 0.3 GJ and 0.06 GJ, respectively. We also estimated the counter single force excited by the 2015 eruptions by using seismic waveform matching of a broadband seismometer. The depths of the counter force by the 2015 eruptions were near sea level. The pulse width and the amount of the force were lined on the scaling line for the initial pressure of 6MPa. The energies of the seismic and acoustic waves of the eruptions and the

source parameter can be related to the intensity of the explosivity of the eruption and the amount of the ejected material. These parameters will be quantified in future studies.

Acknowledgements

We are very grateful to the staff of Sakurajima Volcano Research Center for maintaining the permanent observation system of Kuchinoerabujima Volcano. NIED data have been managed by Drs. Toshikazu Tanada and Hideki Ueda. Fukuoka Regional Headquarters of JMA provided the movies of the 2014 and 2015 eruptions at KEMN station at Kuchinoerabujima. This work was supported by MEXT KAKENHI Grant Number 15H05794 to M.I. and JSPS KAKENHI Grant Number 16K12849 to H.N., and by the Ministry of Education, Culture, Sports, Science and Technology (MEXT) of Japan, under its Earthquake and Volcano Hazards Observation and Research Program. We are grateful to two anonymous reviewers and a sub-editor for their constructive comments and suggestions.

References

- Aoyama, H., 2008. Simplified test on tilt response of CMG40T seismometers, *Bulletin of the Volcanological Society of Japan*, 53, 35–46, (in Japanese with English abstract and captions).
- Arámbula-Mendoza, R., Valdés-González, C., Varley, N., Juárez-García, B., Alonso-Rivera, P., and Hernández-Joffre, V., 2013. Observation of Vulcanian explosions with seismic and acoustic data at Popocatepetl Volcano, Mexico, Dataset found in https://www.researchgate.net/publication/259310972_Observation_of_Vulcanian_explosions_with_seismic_and_acoustic_data_at_Popocatepetl_Volcano_Mexico?ev=prf_pub.
- Bouchon, M., 1979. Discrete wave number representation of elastic wave fields in three-space dimensions, *Journal of Geophysical Research*, 84, 3609–3614.
- Bouchon, M., 1981. A simple method to calculate Green's functions for elastic layered media, *Bulletin of the Seismological Society of America*, 71, 959–971.
- Brocher, T.M., 2005. Empirical relations between elastic wavespeeds and density in the Earth's crust, *Bulletin of the Seismological Society of America*, 95, 2081–2092, doi:10.1785/0120050077.
- Brodsky, E.E., Kanamori, H., and Sturtevant, B., 1999. A seismically constrained mass discharge rate for the initiation of the May 18, 1980 Mount St. Helens eruption, *Journal of Geophysical Research*, 104, 29387–29400, doi:10.1029/1999JB900308.
- Clawson, S.R., Smith, R.B., and Benz, H.M., 1989. P wave attenuation of the Yellowstone Caldera from three-dimensional inversion of spectral decay using explosion source seismic data, *Journal of Geophysical Research*, 94, 7205–722, doi:10.1029/JB094iB06p07205.
- Cruz-Atienza, V.M., Pacheco, J.F., Singh, S.K., Shapiro, N.M, Valdés, C., and Iglesias, A., 2001. Size of Popocatepetl Volcano explosions (1997-2001) from waveform inversion, *Geophysical Research Letters*, 28, 4027–4030, doi:10.1029/2001GL013207.
- Fee, D. and Matoza, R.S., 2013. An overview of volcano infrasound: from Hawaiian to Plinian, local to global, *Journal of Volcanology and Geothermal Research*, 249, 123–139, doi:10.1016/j.jvolgeores.2012.09.002.
- Geshi, N. and Kobayashi, T., 2007. Geological map of Kuchinoerabujima Volcano (1:25,000), Geological map of volcanoes 14, Geological Survey of Japan, AIST, (in Japanese with English captions).
- Geshi, N., Iguchi, M., and Shinohara, H., 2016. Phreatomagmatic eruptions of 2014 and 2015 in the Kuchinoerabujima Volcano triggered by a shallow intrusion of magma, *Journal of Natural Disaster Science*, 37, 2, 67–78.
- Glaze, L.S. and Baloga, S.M., 1996. Sensitivity of buoyant plume heights to ambient atmospheric conditions: Implications for volcanic eruption columns, *Journal of Geophysical Research*, 101, D1, 1529–1540, doi:10.1029/95JD03071.
- Graf, Hans-F., Herzog, M., Oberhuber, J.M., and Textor, C., 1999. Effect of environmental conditions on volcanic plume rise, *Journal of Geophysical Research*, 104, D20, 24309–24320, doi:10.1029/1999JD900498.

- Iguchi, M. et al., 2005. Seismic exploration by using active sources at Kuchinoerabujima Volcano, southwest Japan, *Annals of Disaster Prevention Research Institute, Kyoto University*, 48B, 297–322, (in Japanese with English abstract and captions).
- Iguchi, M., 2016. Method for real-time evaluation of discharge rate of volcanic ash, Case study on intermittent eruptions at the Sakurajima Volcano, Japan, *Journal of Disaster Research*, 111, 4–14.
- Iguchi, M., Nakamichi, H., Tameguri, T., Yamamoto, K., Mori, T., Ohminato, T., and Saito, E., 2017. Contribution of monitoring data to decision making for evacuation from the eruptions in 2014 and 2015 at Kuchinoerabujima Volcano, *Journal of Natural Disaster Science*, 38, 1, 31–47.
- Japan Meteorological Agency, 2014, Major eruptive activities in Japan in 2014, in *Monthly report on earthquakes and volcanoes in Japan*, December 2014, 116–128, (in Japanese).
- Japan Meteorological Agency, 2015, Major eruptive activities in Japan in 2015, in *Monthly report on earthquakes and volcanoes in Japan*, December 2015, 98–110, (in Japanese).
- Johnson, J.B., 2003. Generation and propagation of infrasonic airwaves from volcanic explosions, *Journal of Volcanology and Geothermal Research*, 121, 1–14, doi:10.1016/S0377-0273(02)00480-0.
- Johnson, J.B. and Aster, R.C., 2005. Relative partitioning of acoustic and seismic energy during Strombolian eruptions, *Journal of Volcanology and Geothermal Research*, 148, 334–354, doi:10.1016/j.jvolgeores.2005.05.002.
- Johnson, J.B., Aster, R.C., and Kyle, P.R., 2004. Volcanic eruptions observed with infrasound, *Geophysical Research Letters*, 31, L14604, doi:10.1029/2004GL020020.
- Kanamori, H. and Given, J.W., 1983. Lamb pulse observed in nature, *Geophysical Research Letters*, 10, 373–376, doi:10.1029/GL010i005p00373.
- Kanamori, H., Given, J.W. and Lay, T., 1984. Analysis of seismic body waves excited by the Mount St. Helens eruption of May 18, 1980, *Journal of Geophysical Research*, 89, 1856–1866, doi:10.1029/JB089iB03p01856.
- Kanda, W., Utsugi, M., Tanaka, Y., Hashimoto, T., Fujii, I., Hasenaka, T., and Shigeno, N., 2010. A heating process of Kuchinoerabujima Volcano, Japan, as inferred from geomagnetic field variations and electrical structure, *Journal of Volcanology Geothermal Research*, 189, 158–171, doi:10.1016/j.jvolgeores.2009.11.002.
- Kato, A., Terakawa, T., Yamanaka, Y., Maeda, Y., Horikawa, S., Matsuhira, K., and Okuda, T., 2015. Preparatory and precursory processes leading up to the 2014 phreatic eruption of Mount Ontake, Japan, *Earth Planets and Space*, 67, 111, doi:10.1186/s40623-015-0288-x.
- Kato, K., Oshima, H., and Sasatani, T., 2002. Source mechanism of volcanic explosion earthquakes during the 1988–1989 Mt. Tokachi Eruptions, *Geophysical Bulletin of Hokkaido University, Sapporo, Japan*, 65, 179–198.
- Kennett, B.L. and Kerry, N.J., 1979. Seismic waves in a stratified half space, *Geophysical Journal of the Royal Astronomical Society* 57, 557–583, doi:10.1111/j.1365-246X.1979.tb06779.x.
- Mastin, L.G., Guffanti, M., Servranckx, R., Webley, P., Barsotti, S., Dean, K., Durant, A., Ewert, J.W., Neri, A., Rose, W.I., Schneider, D., Siebert, L., Stunder, B., Swanson, G., Tupper, A., Volentik, A., and Waythomas, C.F., 2009. A multidisciplinary effort to assign realistic source parameters to models of volcanic ash-cloud transport and dispersion during eruptions, *Journal of Volcanology and Geothermal Research*, 186, 10–21, doi:10.1016/j.jvolgeores.2009.01.008.
- Matsuzawa, T., Matsumoto, T., and Tanada, T., 2016. Seismic inversion analysis of the 2014 and 2015 Kuchinoerabujima Volcano eruptions, using F-net broadband seismometers, *Journal of Natural Disaster Science*, 37, 2, 91–103.
- McNutt, S.R., 1994. Volcanic tremor amplitude correlated with the Volcanic Explosivity Index and its potential use in determining ash hazards to aviation, *Acta Vulcanologica* 5, 197–200.
- McNutt, S.R. and Nishimura, T., 2008. Volcanic tremor during eruptions: Temporal characteristics, scaling and constraints on conduit size and processes, *Journal of Volcanology and Geothermal Research*, 178, 10–18, doi:10.1016/j.jvolgeores.2008.03.010.
- Nishimura, T., 1995. Source parameters of the volcanic eruption earthquakes at Mount Tokachi, Hokkaido, Japan, and magma ascending model, *Journal of Geophysical Research*, 100, 12456–12473, doi:10.1029/95JB00867.
- Nishimura, T. and Hamaguchi, H., 1993. Scaling law of volcanic explosion earthquake, *Geophysical Research Letters*, 20, 2479–2482, doi:10.1029/93GL02793.

- Nishimura, T. and Uchida, H., 2005. Application of single force model to the volcanic explosion earthquakes observed at Asama Volcano in 2004, *Bulletin of the Volcanological Society of Japan*, 50, 387–391, (in Japanese with English abstract and captions).
- Ohminato, T. and Chouet, B., 1997. A free-surface boundary condition for including 3D topography in the finite difference method, *Bulletin of the Seismological Society of America*, 87, 494–515.
- Ohminato, T., Chouet, B., Dawson, P., and Kedar, S., 1998. Waveform inversion of very-long-period impulsive signals associated with magmatic injection beneath Kilauea Volcano, Hawaii, *Journal of Geophysical Research*, 103, 23839–23862, doi:10.1029/98JB01122.
- Ohminato, T., Takeo, M., Kumagai, H., Yamashina, T., Oikawa, J., Koyama, E., Tsuji, H., and Urabe, T., 2006. Vulcanian eruptions with dominant single force components observed during the Asama 2004 volcanic activity in Japan, *Earth Planets and Space*, 58, 583–593, doi:10.1186/BF03351955.
- Okada, Y., Kasahara, K., Hori, S., Obara, K., Sekiguchi, S., Fujiwara, H., and Yamamoto, A., 2004. Recent progress of seismic observation networks in Japan –Hi-net, F-net, K-NET, and KiK-net-, *Earth Planets and Space*, 56, 15–28, doi:10.1186/BF03353076.
- Prejean, S.G. and Brodsky, E.E., 2011. Volcanic plume height measured by seismic waves based on a mechanical model, *Journal of Geophysical Research*, 116, B01306, doi:10.1029/2010JB007620.
- Pyle, D.M., 1989. The thickness, volume and grainsize of tephra fall deposits, *Bulletin of Volcanology*, 51, 1–15, doi:10.1007/BF01086757.
- Ripepe, M., Ciliberto, S., and Della Schiava, M., 2001. Time constraints for modeling source dynamics of volcanic explosions at Stromboli, *Journal of Geophysical Research*, 106, 8713–8727, doi:10.1029/2000JB900374.
- Sparks, R.S.J., Bursik, M.I., Carey, S.N., Gilbert, J.S., Glaze, L.S., Sigurdsson, H., and Woods, A.W., 1997. *Volcanic Plumes*, Wiley, Chichester, 574p.
- Takano, K. et al., 2008. Construction of next generation earthquake data exchange and distribution system over the SINET3 nation-wide L2 network, paper presented at Japan Geoscience Union Meeting, Abstract S144-009, Chiba, Japan.
- Tanaka, H.L. and Iguchi, M., 2016. Numerical simulation of volcanic ash plume dispersal from Kuchinoerabujima on 29 May 2015, *Journal of Natural Disaster Science*, 37, 2, 79–90.
- Triastuty, H., Iguchi, M., and Tameguri, T., 2009. Temporal change of characteristics of shallow volcano-tectonic earthquakes associated with increase in volcanic activity at Kuchinoerabujima Volcano, Japan, *Journal of Volcanology Geothermal Research*, 187, 1–12, doi:10.1016/j.jvolgeores.2009.05.017.
- Uhira, K. and Toriyama, N., 2015. Meeting with the May 29, 2015 eruption of Kuchinoerabujima Volcano, *Bulletin of the Volcanological Society of Japan*, 60, 487–490, (in Japanese with English captions).
- Urushidani, S. and Matsukata, J., 2008. Next-generation science information network for leading-edge applications, *Fusion Engineering and Design*, 83, 498–503, doi:10.1016/j.fusengdes.2007.10.003.
- Wilson, L. and Walker, G.P.L., 1987. Explosive volcanic eruptions – VI. Ejecta dispersal in plinian eruptions: the control of eruption conditions and atmospheric properties, *Geophysical Journal of the Royal Astronomical Society*, 89, 657–679, doi:10.1111/j.1365-246X.1987.tb05186.x.
- Yamada, T., Aoyama, H., Nishimura, T., Yakiwara, H., Nakamichi, H., Oikawa, J., Iguchi, M., Hendrasto, M., and Suparman, Y., 2016. Initial phases of explosion earthquakes accompanying Vulcanian eruptions at Lokon-Empung Volcano, Indonesia, *Journal of Volcanology and Geothermal Research*, doi:10.1016/j.jvolgeores.2016.08.011.
- Zobin, V.M., Navarro-Ochoa, C.J., and Ryes-Dávila, G.A., 2006a. Seismic quantification of the explosions that destroyed the dome of Volcán de Colima, Mexico, in July–August 2003, *Bulletin of Volcanology*, 69, 141–147, doi:10.1007/s00445-006-0060-y.
- Zobin, V.M., Navarro-Ochoa, C.J., and Ryes-Dávila, G.A., Orozco, J., Bretón, M., Tellez, A., Reyes-Alfaro, G., and Vázquez, H., 2006b. The methodology of quantification of volcanic explosions from broad-band seismic signals and its application to the 2004–2005 explosions at Volcán de Colima, Mexico, *Geophysical Journal International*, 167, 467–478, doi:10.1111/j.1365-246X.2006.03108.x.